Focal Plane Array of Shaped Quartz Lenses for Wide Field-of-view Sub-millimeter Imaging Systems

Zhang, Huasheng; Dabironezare, Shahab Oddin; Baselmans, Jochem J.A.; Llombart, Nuria

DOI
10.1109/TAP.2023.3334391

Publication date
2023

Document Version
Final published version

Published in
IEEE Transactions on Antennas and Propagation

Focal Plane Array of Shaped Quartz Lenses for Wide Field-of-View Submillimeter Imaging Systems

Huasheng Zhang, *Member, IEEE*, Shahab Oddin Dabironezare, *Member, IEEE*, Jochem J. A. Baselmans, and Nuria Llombart, *Fellow, IEEE*

***Abstract*— Large format focal plane arrays (FPAs) of dielectric lenses are promising candidates for wide field-of-view submillimeter imagers. In this work, we optimize the scanning gain of such imagers via shaping lens surfaces. We develop an optimization procedure using a field correlation technique between the fields generated by a reflector on the top of the lenses and those generated by the lens feeds. Based on this procedure, an FPA of quartz lens antennas combined with leaky-wave feeds is designed to efficiently illuminate the reflector, achieving a directivity of 50.5 dBi up to scanning 20.3°. The obtained scanning gain loss of 2.6 dB is much lower than that associated with the direct fields coming from the reflector (about 6 dB). The proposed FPA is validated by full-wave simulations with excellent agreement. We have fabricated and measured an example shaped quartz lens optimized for the scanning angle of 20.3° at 180 GHz. The comparison between the simulations and the measurements also shows excellent agreement.**

***Index Terms*— Field correlation, focal plane arrays (FPAs), leaky-wave antennas (LWAs), lens antennas, lens shaping, quartz lenses, submillimeter imaging.**

I. Introduction

FOCAL plane arrays (FPAs) are widely considered in the (sub-)THz regime for imaging applications in the areas of astronomy and security [1], [2], [3], [4], [5], [6], [7], [8], [9], [10], [11]. In these applications, FPAs commonly consist of horn arrays, e.g., [1], [8], or lens arrays, e.g., [10], which are coupled with the reflectors. The size of reflector apertures depends on the required resolution and is limited by the need for performing mechanical scanning [12]. In most cases, high aperture efficiency is needed, limiting the possibility of improving the scanning performance via the optimization of shapes of the main reflectors [11]. Here, we consider the application scenario of a state-of-the-art imaging radar discussed in [8]. This imager has a horn-based FPA with an equivalent aperture of $141.4\lambda_0$ (λ_0 is the wavelength) which leads to an estimated broadside directivity of 52 dBi. Because of the limited field shaping capabilities of horns, such a system suffers from a scan loss (SL) of 3 dB at 14°. To further improve the scanning performance, dielectric lens antennas are promising candidates since their shapes can be optimized to synthesize demanded radiation patterns.

Several studies have been carried out to investigate axisymmetric or arbitrarily shaped lenses to synthesize desired radiation patterns [13], [14], [15], [16], [17], [18], [19], [20], [21]. In these works, lens surfaces were optimized locally or globally using geometrical/physical optics (GO-PO), spherical wave expansions, or finite-difference time-domain approaches, depending on the lens size. However, these methods require complex numerical optimization procedures which cannot provide much insight into the analysis of the lens itself. Recently, a coherent Fourier optics (CFO)-based method was presented in [22] to shape silicon lenses coupled to a parabolic reflector. These lenses are analyzed in reception (Rx) and designed according to a direct solution of a field correlation technique. The achieved SL is 1.6 dB at 20.3° which is much lower than that predicted by the direct fields coming from the reflector. However, such study was done only for shallow silicon lenses, which are costly to fabricate.

In this work, we instead explore whether similar performance can be achieved by lenses with lower permittivity, in particular made of quartz with $\varepsilon_r = 3.75$. In [22], the optimized shapes of the shallow silicon lenses were derived directly from the plane wave (PW) spectrum of the reflector–lens combination without the need of optimization procedures. However, in the case of nonshallow lenses, due to more significant effects associated with the total reflection beyond the critical angle, an optimization procedure is needed. Therefore, in this work, we have developed a specific method that correlates the reflector's focal fields and the radiated fields of the lens antennas over the lens aperture planes. This choice allows for evaluating the reflector's focal fields only once outside the optimization cycle leading to faster optimization.

The lens feed is a resonant leaky-wave antenna (LWA) with a double-slot iris [23]. Such a feed is particularly efficient in illuminating dielectric lenses and can be easily integrated

Manuscript received 22 June 2023; revised 25 October 2023; accepted 9 November 2023. Date of publication 28 November 2023; date of current version 15 February 2024. This work was supported by the European Research Council Starting Grant, ERC-2014-StG LAA-THz-CC, under Grant 639749. *(Corresponding author: Huasheng Zhang.)*

Huasheng Zhang, Shahab Oddin Dabironezare, and Nuria Llombart are with the Terahertz Sensing Group, Microelectronics Department, Delft University of Technology, 2628 CD Delft, The Netherlands (e-mail: h.zhang-12@tudelft.nl; dabironezare.shahab@ieee.org; n.llombartjuan@tudelft.nl).

Jochem J. A. Baselmans is with the SRON Netherlands Institute for Space Research, 2333 CA Leiden, The Netherlands, and also with the Terahertz Sensing Group, Microelectronics Department, Delft University of Technology, 2628 CD Delft, The Netherlands (e-mail: j.baselmans@sron.nl).

Color versions of one or more figures in this article are available at https://doi.org/10.1109/TAP.2023.3334391.

Digital Object Identifier 10.1109/TAP.2023.3334391

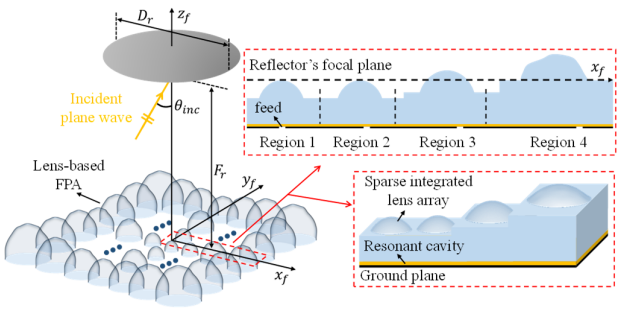

Fig. 1. Architecture of the proposed lens-based FPA. The top inset shows the lens elements in the four regions identified in [22]. The bottom inset depicts the structure of the integrated lens array.

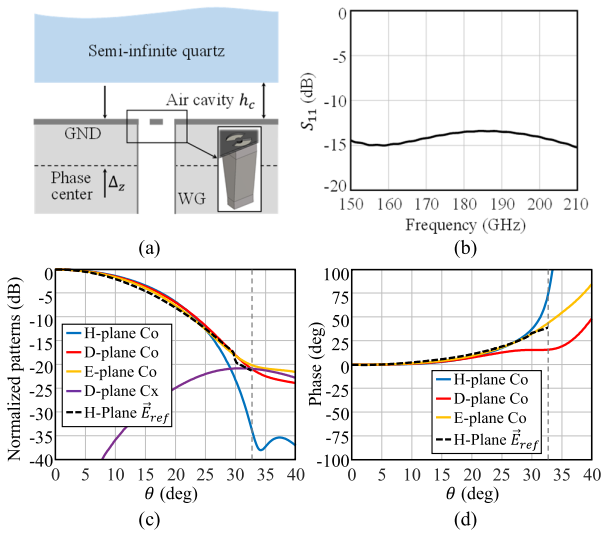

Fig. 2. (a) Structure of the lens feed for the FPA: a resonant LWA. A double-slot iris is fed by a waveguide and radiated toward the semi-infinite quartz medium through an air cavity. The inset shows the 3-D feed geometry in [24]. WG: waveguide. (b) Simulated S-parameter of the feed. (c) and (d) Amplitude and phase of the field radiated by the LWA feed, respectively. This field is plotted at 180 GHz inside the quartz medium on a sphere with the radius of $8\lambda_d$. The dashed black curve represents the reflector's scattered field, $\vec{E}_{ref}$, on the same sphere for the broadside incidence case. The dashed gray lines represent the optimized lens truncation angle θ_0^l.

with lenses. We first briefly discuss the lens optimization with this feed for moderate scanning angles, and then mainly focus on the optimization procedures for large scanning angles by shaping lens surfaces. Shaped lens surfaces can compensate the higher order phase aberrations present in reflector's focal fields and achieve better field correlation. We present an example design of the shaped quartz lens at the edge of the FPA for a scanning angle of 20.3° at 180 GHz. The optimized lens couples well to the reflector, and the system achieves a scanning directivity of 50.5 dBi with a scanning gain loss of 2.6 dB. This performance is compared with the state-of-the-art showing low SL while maintaining high broadside aperture efficiency. A prototype of this shaped quartz lens was fabricated using the same waveguide feed as in [24]. We have measured the lens radiation performance, and it is in excellent agreement with the simulations.

This article is organized as follows. Section II introduces the considered imaging scenario and the geometry of the lens feed. Section III describes the proposed field correlation method and the optimization procedures for different scanning angles. Section IV discusses the optimization of the lens geometries when the scanning angle is moderate. Section V discusses the procedures to modify lens surfaces when the scanning angles are large and shows an example design of the edge lens element. Its performance is analyzed, validated, and compared with the state-of-the-art. Section VI shows the prototype and the measurement results.

II. Imaging Scenario

Let us consider the imaging scenario shown in Fig. 1. An array of quartz lenses is placed at the focal plane of a main reflector which is illuminated by an incident PW with the incident angle of $(\theta_{inc}, \phi_{inc})$. For simplicity, the main reflector aperture is modeled as a symmetric nonoversized parabola, but it can be easily extended to more practical components. We consider the central frequency as 180 GHz. The reflector has a diameter of $D_r = 141.4\lambda_0$, a focal distance of $F_r = 282.8\lambda_0$, and an f-number of $f_\#^r = F_r/D_r = 2$, which are in line with the reflector dimensions in [8] and [22].

For the described FPA, the antenna feeds are placed over a flat surface, enabling monolithic integration at high frequencies, as shown in the top inset in Fig. 1. The lens feeds remain the same across the array while the lens geometries change for different scanning angles. To facilitate the design of lenses in a large format FPA, we discretize the FPA into four regions as suggested in [22]. The corresponding lens geometries are depicted in the top and bottom insets in Fig. 1. In the first three regions, lens surfaces are elliptical. As the scanning angle increases, the lens diameters increase, and the lens feeds are displaced with respect to lens focuses. While in the fourth region, the shapes of lens surfaces need to be modified to compensate the higher order phase terms present in the reflector's focal fields. The FPA is not fully sampled, and its sampling size follows that used in [8] where a mechanical scanner was used to fulfill the complete field of view.

In this work, we consider a resonant LWA as the lens feed, and its stratification is shown in Fig. 2(a). A resonant air cavity is placed between the ground plane and the lens material to enable the excitation of leaky waves. On the ground plane, a double-slot iris is excited by a square waveguide. To facilitate the fabrication and measurement, here we use the same iris and waveguide dimensions as discussed in [24]. In our case, the stratification dimensions are different: $h_c = 0.48\lambda_0$ and $\Delta z = 0.87\lambda_0$. This LWA was simulated in CST [25] full-wave simulator when radiating toward semi-infinite quartz medium, see Fig. 2(a). The S-parameter of the antenna is shown in Fig. 2(b) and it shows very good impedance matching over a wide bandwidth. Fig. 2(c) and (d) shows the field radiated by the feed inside the lens medium at 180 GHz over a sphere with the radius of $8\lambda_d$ (λ_d: wavelength inside the medium). This radiated field will be used to decide the lens truncation angle and will be discussed in detail in Section IV.

III. Field Correlation Optimization Technique

To find the optimized lens shape for each scanning direction, we propose to use a field correlation technique between the

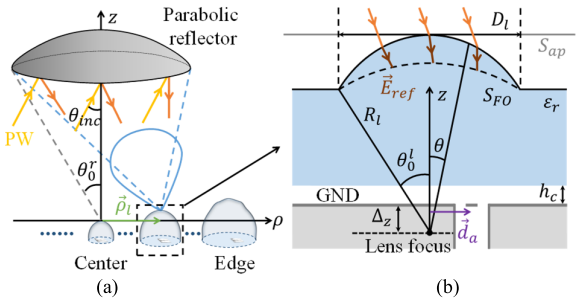

Fig. 3. (a) Schematic representation of a scenario when a PW illuminates the reflector and couples to one of the lens elements in the FPA. The blue beam represents the radiated field of the lens antenna in the transmission mode. (b) Detailed structure of the lens antenna.

reflector's focal fields and the lens radiated fields, similar to the method discussed in [26]. Let us consider the scenario depicted in Fig. 3(a). An incident PW is coming from a certain direction $(\theta_{inc}, \phi_{inc})$. It is scattered by the reflector and couples to the lens antenna located at $\vec{\rho}_l$ in the focal plane of the reflector. The detailed lens geometry is shown in Fig. 3(b). Here, we consider an elliptical lens with the diameter D_l, the rim distance R_l (corresponds to the truncation angle θ_0^l), and the lens f-number $f_\#^l = R_l/D_l$. The phase center of the feed is placed at the lens focal plane and the feed lateral position is displaced $\vec{d}_a$ with respect to the lens focus.

Each lens in the FPA is optimized to maximize the aperture efficiency η_{ap} of the reflector for a specific PW direction. This efficiency can be defined as the ratio of the power received by the lens feed, $P_r(\theta_{inc}, \phi_{inc})$, under the impedance-matched condition, to the power incident onto the reflector, P_{inc}^{PW}, at broadside

$$\eta_{ap}(\theta_{inc}, \phi_{inc}) = \frac{P_r(\theta_{inc}, \phi_{inc})}{P_{inc}^{PW}} \tag{1}$$

where $P_{inc}^{PW} = 0.5|E_0|^2 A_{ref}/\zeta_0$, A_{ref} is the physical area of the reflector, and E_0 is the amplitude of the PW electric field. The power $P_r(\theta_{inc}, \phi_{inc})$ in (1) can be evaluated using a field correlation integral between the incident field scattered from the reflector to an arbitrary surface S and the field radiated by the lens feed on the same surface [27], either inside or outside the lens. This power is expressed as follows:

$$P_r(\theta_{inc}, \phi_{inc}) = \frac{1}{16 P_{rad}^{LWA}} \left| \iint_S \vec{H}_{LWA}(\vec{r}) \cdot \vec{M}_{inc}(\vec{r}, \theta_{inc}, \phi_{inc}) - \vec{E}_{LWA}(\vec{r}) \cdot \vec{J}_{inc}(\vec{r}, \theta_{inc}, \phi_{inc}) dS \right|^2 \tag{2}$$

where $[\vec{E}_{LWA}(\vec{r}), \vec{H}_{LWA}(\vec{r})]$ is the field radiated by the LWA on the surface S in the transmission (Tx) mode. $\vec{M}_{inc} = \vec{E}_{ref} \times \hat{n}$ and $\vec{J}_{inc} = \hat{n} \times \vec{H}_{ref}$ are the equivalent currents evaluated using the field scattered by the reflector on the same surface, i.e., $[\vec{E}_{ref}(\vec{r}), \vec{H}_{ref}(\vec{r})]$.

To maximize η_{ap} in (1), we need to optimize the integrand in (2), and this can be done by conjugately matching $[\vec{E}_{LWA}, \vec{H}_{LWA}]$ with $[\vec{M}_{inc}, \vec{J}_{inc}]$. In previous works [22], [24], [28], this field correlation was performed on an equivalent sphere inside the lens, i.e., S_{FO} in Fig. 3(b). Particularly in [22], the scattered reflector's fields have to be propagated to this sphere using a GO method in combination with an FO method. Such procedures are useful to design the lens geometries in region 1; however, for larger scanning angles, it is more convenient to use an equivalent aperture on the top of the lens surface for evaluating (2), i.e., S_{ap} in Fig. 3(b). In this way, the scattered fields of the reflector are only computed once outside the multiparametric optimization loop. In different regions (see Fig. 1), different parameters of lens antennas are optimized as follows.

1) Region 1: elliptical lens geometry (D_l, $f_\#^l$). The same geometry is used in the entire region.
2) Region 2: the location of the feed inside the lens, $\vec{d}_a$. The elliptical lens geometry is kept the same.
3) Region 3: $\vec{d}_a$ increases and D_l is enlarged (a limit is set to $10\lambda_0$). The same $f_\#^l$ is kept.
4) Region 4: $\vec{d}_a$, D_l, and the shape of lens surface (via Zernike polynomials) change. The same $f_\#^l$ is kept.

This procedure is done in MATLAB using its global optimization tool which runs parametric analysis for all the mentioned parameters, with the goal of maximizing (1). The explicit optimization for each region and the corresponding results will be shown in Sections IV and V.

IV. Lens Antenna Optimization for Moderate Scanning Angles

The above-mentioned regions in Fig. 1 are only related to the geometry of the reflector, and approximate formulas were given in [22] for the region limits. For our considered imaging scenario, the region limits defined in terms of the number of beams (half-power beamwidth) are: $N_1 = 8.8$, $N_2 = 15.5$, and $N_3 = 23.6$, which corresponds to scanning angles of $\theta_{inc} = N\lambda_0/D_r = 3.6°$, $6.3°$, and $9.6°$. In the first three regions, the lenses have elliptical shapes, and the optimization of their geometries is discussed in this section.

A. Lens Design in Region 1

In the first region, all the lenses are identical so we only consider the central lens design. The diameter of the lens is designed to be $D_l = 4.4\lambda_0$ which corresponds to -20 dB truncation of the reflector's focal field on the lens FO sphere, S_{FO}. The f-number of the lens $f_\#^l$ is obtained by maximizing (2) when the field correlation surface is S_{FO}. The optimal $f_\#^l = 0.925$ ($\theta_0^l = 32.7°$) leads to an excellent field matching between the field radiated by the LWA on S_{FO}, i.e., $\vec{E}_{LWA}$, and the reflector's scattered field on S_{FO}, i.e., $\vec{E}_{ref}$, as shown in Fig. 2(c) and (d). Note that $\vec{E}_{LWA}$ has to be evaluated in the near-field with $R_l = 8\lambda_d$ since the lens is small [29]. The amplitude is symmetric in all the planes and the phase is almost constant until 25°. Here, we implement a quarter-wavelength matching layer made of Parylene ($\varepsilon_r = 2.62$) on the lens surface to improve the transmission between the quartz–air interface by about 0.5 dB.

We also evaluate the far-field radiated by this lens. This field is calculated using an in-house PO code [28] and shown in Fig. 4. The pattern is symmetric and illuminates the reflector with -10 dB amplitude taper at the reflector's rim where

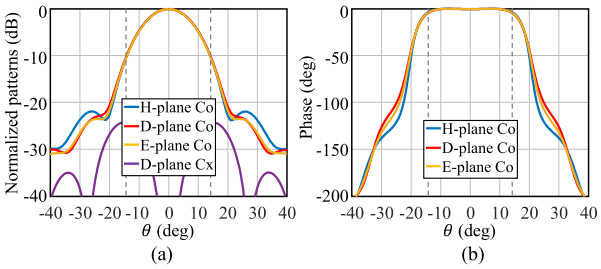

Fig. 4. Secondary far-field radiated by the lens antenna toward the reflector: (a) amplitude and (b) phase. The dashed gray lines represent the reflector truncation angle θ_0^r. A quarter-wavelength matching layer ($\varepsilon_r = 2.62$) is used.

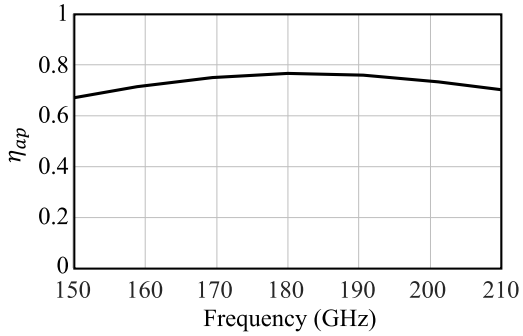

Fig. 5. Optimized aperture efficiency η_{ap} of the reflector coupled to the central lens with $D_l = 4.4\lambda_0$ and $f_\#^l = 0.925$. A quarter-wavelength matching layer ($\varepsilon_r = 2.62$) is used.

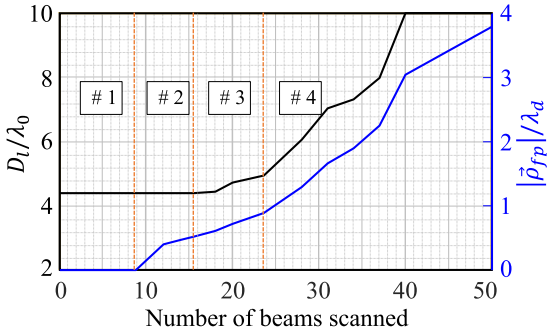

Fig. 6. Flash point $\vec{\rho}_{fp}$ and lens diameter D_l versus the number of beams scanned. The orange lines show the border of the four regions of the FPA.

$\theta_0^r = 14.25°$ (shown by the dashed gray lines). Moreover, the phase within the relevant angle is almost constant. The resulting aperture efficiency of the lens–reflector system, η_{ap}, is plotted in Fig. 5 versus frequencies. It shows broadband behavior and the value at 180 GHz is 76.7% which is comparable to the performance of the design based on silicon lenses [22].

B. Lens Optimization in Regions 2 and 3

The lens f-number remains the same as $f_\#^l = 0.925$ for lenses in all the regions. In region 2, the lens diameters are still $D_l = 4.4\lambda_0$ but in region 3 they are enlarged to follow the reflector's focal fields [22] (with a limitation on the maximum lens diameter of $10\lambda_0$). Fig. 6 shows the variation in D_l as a function of the number of beams scanned.

Starting from region 2, the phase term introduced by the nonbroadside PW in the reflector aperture presents a significant linear term in $\vec{E}_{ref}$. Therefore, the feed should be displaced along the focal plane of the lens to add an extra phase term in $\vec{E}_{LWA}$ to compensate the incident linear phase. An estimation of the feed displacement $\vec{d}_a$ can be obtained using the ray tracing approximation. We can consider a PW arriving at the lens with an incident angle of $(\theta_{inc}, \phi_{inc})$. Using Snell's law, the position where these transmitted rays are focused, also referred to as the flash point, can be estimated as follows:

$$\vec{\rho}_{fp} = \frac{f_\#^l D_l}{1-e}\left[1 - e\cos\left(\sin^{-1}\frac{1}{2f_\#^l}\right)\right] \cdot \tan\left[\sin^{-1}(e\sin\theta_{inc})\right]\left(\cos\phi_{inc}\hat{x} + \sin\phi_{inc}\hat{y}\right) \quad (3)$$

where $e = 1/\sqrt{\varepsilon_r}$ is the lens eccentricity. $\vec{\rho}_{fp}$ is also plotted in Fig. 6 and we can note it increases significantly as the scanning beam increases. By parametrically sweeping $\vec{d}_a$ and D_l around their estimated values, we can obtain the optimal lens geometries in regions 2 and 3.

For the optimized lenses in regions 1–3, we have evaluated their SL when coupled to the reflector, as shown by the solid blue curve in Fig. 7. The crosses in the figure represent the results obtained using the full-wave simulations in CST for the respective quartz lens antennas and TICRA tools, GRASP [30], for the reflector. The agreement between the full-wave simulations and our method is excellent within the first three regions. As a reference, one can evaluate the intrinsic SL associated with the reflector's focal fields. In this case we assume $S \to 0$ and neglect any effect from the lens antennas. This is equivalent as evaluating the decay of the directivity of the incident focal fields [22]. These fields are evaluated using a PO code and their scanning directivity loss is shown by the gray curve in Fig. 7. As the scanning beam increases, the SL of the focal fields is becoming higher than the lens case.

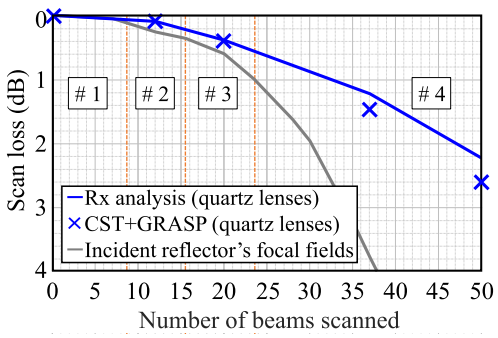

Fig. 7. SL of the lens-coupled reflector versus the number of beams scanned. The solid line represents the SL calculated using the Rx analysis in (2), while the crosses are the results obtained from the full-wave simulations in the Tx mode. As a reference, the SL associated with the reflector's focal fields is shown by the gray curve. The orange lines show the border of the four regions of the FPA.

V. Lens Antenna Optimization for Large Scanning Angles

In region 4 ($\theta_{inc} \geq 9.6°$), the incident PW can be scattered and focused outside the reflector's rim, as shown in Fig. 8(a). In this region, the focal fields are severely distorted and present severe phase aberrations. Let us consider a PW with an incident angle of $\theta_{inc} = 50\lambda_0/D_r = 20.3°$ (scanning 50 beams) as an illustrative example. The reflector's focal

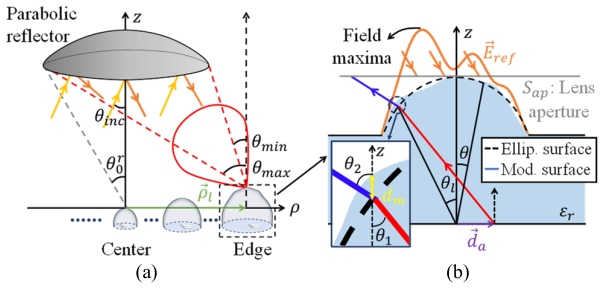

Fig. 8. Edge lens element of the FPA couples to the reflector illuminated by a PW with a large scanning angle. The red beam represents the radiated field of the lens antenna in the Tx mode. (b) Geometry of the shaped edge lens, with an illustration of the ray propagation from the feed. The reflector's focal field $\vec{E}_{ref}$ is also illustrated by the orange curve and rays.

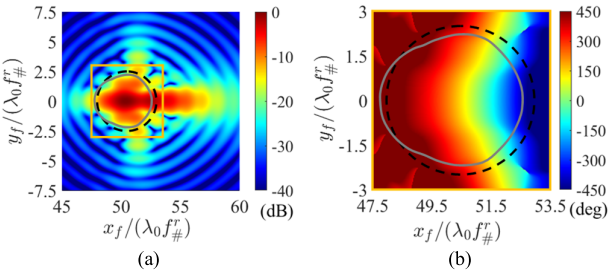

Fig. 9. Reflector's focal field $\vec{E}_{ref}$ at the top of the lens for an incident angle of $\theta_{inc} = 20.3°$: (a) amplitude and (b) phase. The dashed black circle represents the lens area, while the solid gray curve is the lens aperture plane S_{ap}. The area within the orange box in (a) is zoomed in and shown in (b) for the phase variation.

field on the lens aperture plane, $\vec{E}_{ref}$, is shown in Fig. 9. The lens diameter is enlarged to $10\lambda_0$ and its area is marked by the black dashed circle. Fig. 9(b) shows the zoomed-in phase pattern of the focal field in Fig. 9(a). We can see the amplitude is quite distorted with almost two maxima, and the phase varies significantly over the lens aperture. Thus, it would be very difficult for an elliptical lens to generate a matched pattern. For such a case, the elliptical lens surface must be modified to compensate the phase distortion in $\vec{E}_{ref}$, as graphically illustrated in Fig. 8(b). In this section, the optimization procedures for shaping the lens surfaces in region 4 are discussed.

A. Lens Surface Modification

The main objective of the lens surface modification is the phase matching between $(\vec{E}_{LWA}, \vec{H}_{LWA})$ and $(\vec{J}_{inc}, \vec{M}_{inc})$ in (2). The phase difference between these fields, i.e., the phase of the entire integrand in (2), is referred to as the hologram phase, Φ_{holo}^{ellip}. Here, we consider an elliptical lens with its feed displaced according to Fig. 6. In this case, a linear phase is already achieved in $(\vec{E}_{LWA}, \vec{H}_{LWA})$ by the feed displacement. Therefore, Φ_{holo}^{ellip} mainly represents higher order phase aberrations.

To compensate such phase aberrations, we can change the phase distribution of $(\vec{E}_{LWA}, \vec{H}_{LWA})$ by adding a certain thickness d_m in the vertical axis $\hat{z}$ to the original elliptical surface, as depicted in the inset in Fig. 8(b). Such surface modification leads to extra phase propagation of $(\vec{E}_{LWA}, \vec{H}_{LWA})$ in the vertical direction: $\Delta\Phi_{ap}^a = -k_d \cos\theta_1 d_m + k_0 \cos\theta_2 d_m$, where

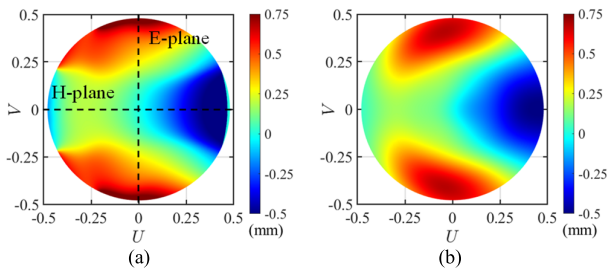

Fig. 10. Optimized lens surface modification: (a) ideal one and (b) smoothed Zernike surface.

k_0 and k_d are the propagation constants in free space and the lens medium, respectively; θ_1 and θ_2 are the incident and transmitted angles with respect to the $\hat{z}$-axis, respectively. By imposing the new hologram phase to be 0, i.e., $\Phi_{holo}^{ellip} + \Delta\Phi_{ap}^a = 0$, we can derive the lens surface modification as follows:

$$d_m(\theta, \phi) = \frac{\Phi_{holo}^{ellip}(\theta, \phi)}{k_d \cos\theta_1 - k_0 \cos\theta_2}. \tag{4}$$

Note that d_m represents the ideal surface modification and it will lead to 100% phase matching in (2). However, directly using (4) can lead to lens modification with rapid changes in the vertical direction due to the jump of phase, especially for nonshallow lenses. This behavior is illustrated by an example shown in Fig. 10(a). Here, the lens modification is optimized for the case of $\theta_{inc} = 20.3°$. We can observe significant height (phase) variation at the edge of the E-plane. This will have strong distortion of the far-field radiated by the lens.

To obtain a smoother surface with a unique tangent plane at every point, we approximate d_m using a Zernike polynomial expansion with a certain number of modes M and N, Z_N^M [31]. This Z_N^M is then added on the top of the elliptical surface Z_l^{ellip} to obtain the shaped lens surface Z_l^{mod} as follows:

$$Z_l^{mod}(\theta, \phi) = Z_l^{ellip}(\theta) + Z_N^M(\theta, \phi) = \frac{a\left(1 - e^2\right)\cos\theta}{1 - e\cos\theta} + \sum_{m=0}^{M} \sum_{n=m}^{N} \left[A_n^m O_n^m(\sin\theta, \phi) + B_n^m E_n^m(\sin\theta, \phi)\right] \tag{5}$$

where a is the semi-major axis of the elliptical lens; O_n^m and E_n^m are the odd and even Zernike polynomials, respectively; and A_n^m and B_n^m are the corresponding weights which are calculated by projecting $d_m(\sin\theta, \phi)$ on these orthogonal polynomials. For a specific d_m, we can tune the values of (M, N) to obtain a more accurate expansion. For d_m in Fig. 10(a), the optimized Zernike modes are $M = 24$, and $N = 2$, and the approximate surface is shown in Fig. 10(b). This surface is smoother and leads to 93% phase matching.

In region 4, the optimization procedures are described as follows. For each set of D_l and $\vec{d}_a$, we first evaluate the ideal modification d_m using (4), and then smooth d_m with a Zernike expansion Z_N^M to create a modified surface Z_l^{mod} using (5). We parametrically optimize the mode number (M, N) to maximize η_{ap} with the modified lens. Note that here we only change the mode number. The weights A_n^m and B_n^m are decided

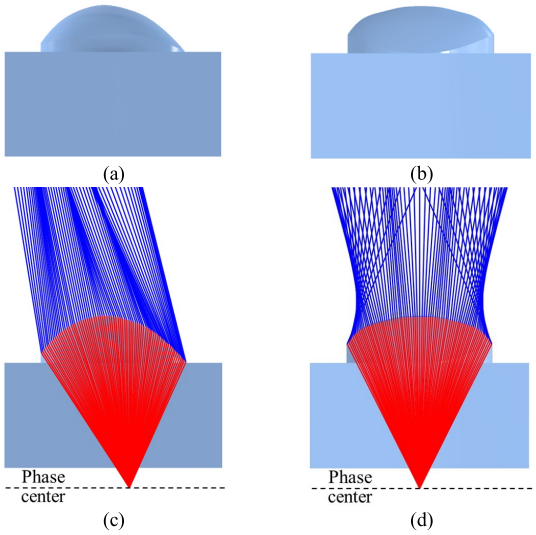

Fig. 11. Optimized shaped lens surface: (a) and (b) surfaces viewed in the H- and E-planes, respectively. (c) and (d) Corresponding ray tracing when the antenna is in the Tx mode. The red and blue rays correspond to the rays inside and outside of the lens, respectively.

according to d_m and they are not optimized individually. Finally, we change the combination of D_l and $\vec{d}_a$ and redo the steps, until a maximum η_{ap} is obtained.

B. Application Case of 50 Beams' Scanning

Let us consider the most challenging lens design for our imaging scenario, i.e., the edge lens element of the FPA coupled to the PW with $\theta_{inc} = 20.3°$. This lens is located outside the reflector's rim with the displacement of $\vec{\rho}_l = +50.47\lambda_0 f_\#^r \hat{x}$ from reflector's focus which corresponds to the rim angles of $\theta_{min} = 6.2°$ and $\theta_{max} = 31.5°$; see Fig. 8(a). The optimized lens parameters are $D_l = 10\lambda_0$, $\vec{d}_a = +2.11\lambda_d \hat{x}$, $M = 24$, and $N = 2$, and the modified lens surface is shown in Fig. 11(a) and (b) for the H- and E-plane side views, respectively. The shaped surface is asymmetric and significantly different from the original ellipsoid. We also plot the ray tracing in Fig. 11(c) and (d) where the red and blue rays correspond to the radiation of the antenna feed inside and outside the lens in the Tx mode, respectively. The transmitted rays outside the lens point toward 16.2° as shown in Fig. 11(c), but due to lens modification, the rays are not well-collimated in Fig. 11(d) and those at the lens edge radiate toward unexpected directions.

Moreover, the lens radiated electric field, $\vec{E}_{LWA}$, on the lens aperture, S_{ap}, is plotted in Fig. 12. Here, we use the same zoomed-in orange area in Fig. 9 to show the field. The lens area is marked by the black dashed circle and the plane S_{ap} where the field correlation in (2) is performed is marked by the solid gray area. This area is not circular due to the tilted propagation of the field by the displaced feed through the modified lens surface. Compared with the reflector's focal field $\vec{E}_{ref}$ in Fig. 9, the amplitude of $\vec{E}_{LWA}$ matches well with that in Fig. 9(a) and its phase is conjugate to that in Fig. 9(b). As a result, this shaped lens can couple best to the reflector with the optimized $\eta_{ap} = 46\%$ and the SL of this case is 2.2 dB

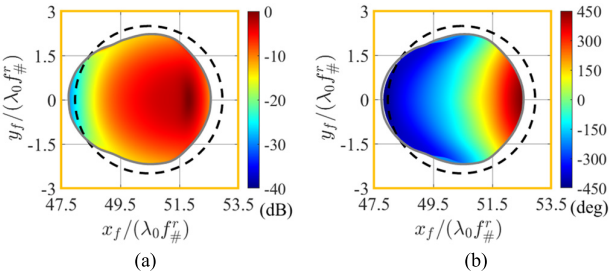

Fig. 12. Lens GO field on the lens aperture S_{ap} within the orange area depicted in Fig. 9: (a) amplitude and (b) phase.

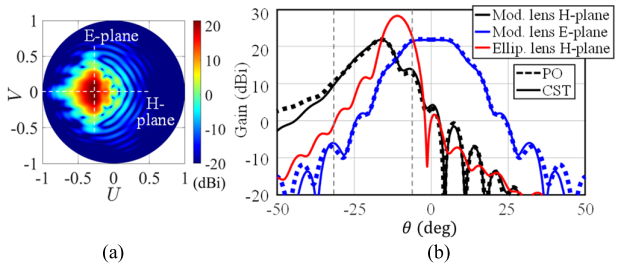

Fig. 13. Secondary far-fields radiated by the optimized shaped lens toward the reflector at 180 GHz: (a) full-wave co-pol pattern shown in the UV plane and (b) comparison of the co-pol patterns between the PO approach and the full-wave simulation in the H-plane (scanning plane) and E-plane. The field radiated by an elliptical lens with the same diameter is also shown as a reference. The dashed gray lines mark the rim angles $\theta_{min} = 6.2°$ and $\theta_{max} = 31.5°$ of the reflector in the H-plane.

which is shown in Fig. 7. This value is much lower than that of the reflector's focal field which is about 6 dB.

C. Far-Field of the Lens-Coupled Reflector for 50 Beams' Scanning

The far-field radiated by the mentioned shaped lens is calculated using the in-house PO code in the Tx mode and is compared with the full-wave simulation where the complete lens plus feed geometries were modeled and simulated. Here, the dielectric loss of quartz is not included in the simulation. The gain of the lens antenna is the product between its directivity and the lens radiation efficiency which includes the feed spillover efficiency within the lens angular domain and the reflection efficiency through the lens surface. Fig. 13(a) shows the copolar secondary field (from CST) in the UV plane at 180 GHz, while Fig. 13(b) shows plots of the cuts along the H-plane (scanning plane) and the E-plane. We can observe excellent agreement between the PO approach and the full-wave simulation within the reflector's rim, i.e., the gray dashed lines. The patterns are asymmetric in the scanning plane and point toward 16.2°. The maximum cross-pol level normalized to the co-pol maxima is below −18 dB at 150 GHz (largest value) and −21 dB at 180 GHz, similar to the values reported in [24]. The optimization via the field correlation method ensures that this pattern illuminates and couples well to the reflector. For comparison, the pattern of an elliptical lens (without the surface modification) with the same diameter is also shown. It is more directive and has a much higher gain because this shape couples better to the LWA feed; however, this field does not couple well to the reflector, as predicted

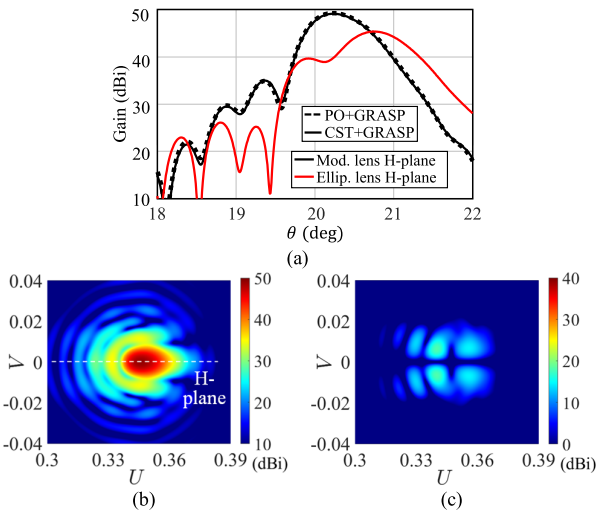

Fig. 14. Far-fields radiated by the lens-coupled reflector at 180 GHz: (a) comparison of the co-pol patterns between the PO approach and the full-wave simulation in the H-plane, (b) full-wave co-pol pattern shown in the UV plane, and (c) cross-pol pattern.

by the field correlation and will be shown in the following. It is worth mentioning that the full-wave simulation took about 5 h to simulate this shaped lens, while our method took about 5 min on the same PC, i.e., 60 times faster.

The far-fields of the reflector are evaluated using the commercial PO code in GRASP. We import the lens secondary fields into GRASP as a tabulated source and radiate it toward the reflector. The resulting reflector's far-fields at 180 GHz are shown in Fig. 14 where (a) shows plots of the co-pol patterns in the H- (scanning) plane; (b) and (c) shows plots of the co-pol and cross-pol patterns (CST+GRASP) in the UV plane, respectively. The maximum cross-pol level normalized to the co-pol maxima is below −25 dB at 150 GHz (largest value) and −30 dB at 180 GHz. As expected, the shaped lens achieves a more directive beam and its gain is about 4 dB higher than that of the elliptical lens. Moreover, the reflector with the shaped lens points toward 20.3° which corresponds to the intended scanning angle θ_{inc}. The agreement between the PO method and the full-wave simulation is excellent. From these far-fields we can also evaluate the directivity and the aperture efficiency of the reflector. With the shaped lens, $Dir^{PO} = 50.6$ dBi, $\eta_{ap}^{PO} = 42.8\%$, $Dir^{CST+GRASP} = 50.5$ dBi, and $\eta_{ap}^{CST+GRASP} = 41.3\%$; while for the elliptical lens, $Dir^{CST+GRASP} = 46.2$ dBi and $\eta_{ap}^{CST+GRASP} = 17.4\%$ which are much lower. The corresponding SL for the shaped lens is $SL^{CST+GRASP} = 2.6$ dB and is shown in Fig. 7 by the cross at 50 beams.

D. SL Versus the Number of Scanned Beams

By following the described optimization procedures, we have designed the lens antennas in all the regions and plotted the SL of the FPA in Fig. 7. The agreement between our Rx analysis and the full-wave simulations is excellent in all the regions. The full-wave SL is slightly higher in region 4 because of the significant surface modification of the quartz lenses. Such modification leads to shadow regions

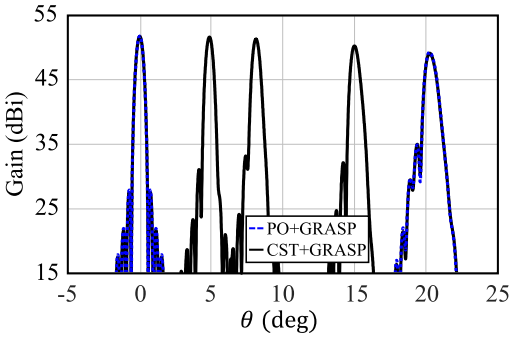

Fig. 15. Far-fields radiated by the reflector in the H-plane for different scanning angles. The reflector is illuminated by the optimized quartz lenses placed in the H-plane. Comparison between the PO results and the full-wave results is also shown for the broadside and the 20.3° scanning cases.

which slightly decrease the lens radiation efficiency and makes the field correlation more difficult. Even though this FPA achieves much better SL than the reflector's incident focal fields when scanning at large angles. We also plot the far-fields radiated by the reflector in Fig. 15 (H-plane) for different lens elements. We can see the far-fields become more and more distorted as the scanning angle increases. This distortion leads to a drop in the gain of the scanned beams with respect to the broadside beam which is equivalent to the reported SL values. In addition, the agreement between the PO results and the full-wave results is excellent.

As a comparison, the simulated/measured performance of the state-of-the-art FPAs is listed in Table I. For a horn-based FPA, if the surfaces of the primary reflectors are not modified, the horns need to be tilted and arranged along a curved focal plane to better couple to the reflector [11]. This will lead to a high broadside aperture efficiency η_{ap} of the reflector, but the SL is limited by the shapes of the horn's radiation patterns. To further improve the scanning performance, a commonly used approach is to modify the shapes of the primary reflectors according to a ray tracing or a GO-based method [9], [32], [33], [34]. At the same time, the curved focal planes are optimized for the shaped reflectors. This will indeed lead to very low SL when scanning to large angles [32], [33]; however, the compromise is the much lower η_{ap}. On the contrary, the proposed shaped lens achieves a low SL of 2.6 dB when scanning to 20.3° while keeping a high broadside η_{ap} of 75%, without shaping the primary reflector. Moreover, in this work, the lenses are placed on a flat focal plane, enabling easier monolithic integration at high frequencies.

VI. Antenna Prototype and Measurement

We have fabricated and measured a prototype to validate the proposed concept of lens shaping. Here, we consider the edge lens design discussed in Section V-B and shown in Fig. 11, and the LWA feed is described in Section II.

A. Antenna Prototype

The fabricated quartz lens antenna is shown in Fig. 16(a). It consists of three parts: the double-slot iris feed [see Fig. 16(b)], the waveguide block which is tapered

TABLE I
SIMULATED/MEASURED PERFORMANCE OF THE STATE-OF-THE-ART FPAS

References	This work sim. / meas.	[9] sim.	[11] sim. / meas.	[32] sim.	[33] sim. / meas.	[34] sim. / meas.
Frequency (GHz)	180	30	220	12.75	500	76.5
D_r (λ_0)	141.4	80	168.7	195 × 186	223.3	23
Broadside Dir. (dBi)	52.5	46	≈ 54	54.3	55.3	≈ 35.9
Scan loss (dB)	2.6/2.6 at 20°	≈ 3.7 at 15°	3 at 12.3°	0.25 at 20°	1.2 at 25.4°	0.54/≈ 1.1 at 13.5°
Broadside θ_{3dB} (deg)	0.46	≈ 2.1	0.5/0.5	≈ 0.4	0.25/0.25	≈ 3/≈ 3.2
Broadside η_{ap}	0.75	0.8	≈ 0.8	0.58	≈ 0.36	0.67
Method	- Shaped lenses - Flat FPA	- Shaped reflectors - Flat horn FPA	-Dragonian reflectors - Curved horn FPA	- Shaped reflectors - Curved horn FPA	- Shaped reflectors - Flat FPA (tilted horns)	- Reflect arrays - Curved horn FPA

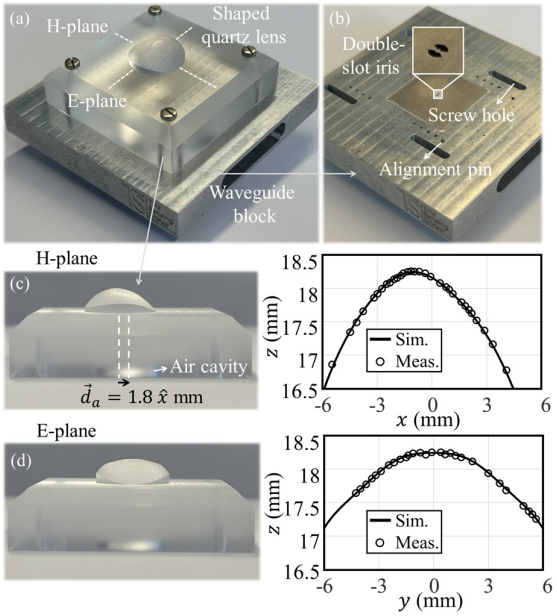

Fig. 16. (a) Photographs of the fabricated quartz lens antenna. (b) Details of the waveguide block, including the double-slot iris feed, the alignment pins, and the screw holes. (c) and (d) Side views of the shaped quartz lens and the corresponding surface profiles compared with the designed shapes. The air cavity and the feed displacement are also shown.

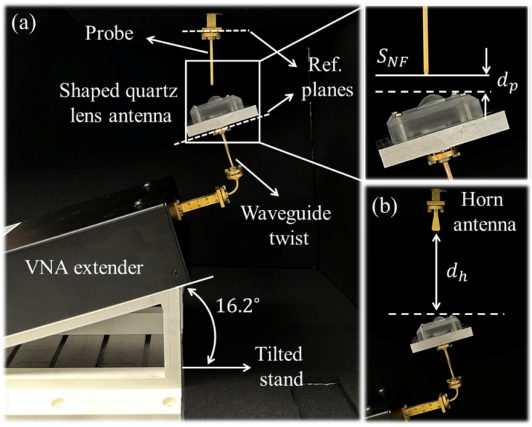

Fig. 17. (a) Measurement setup for the shaped quartz lens antenna. The antenna is fed by a VNA extender through a waveguide twist. The extender is mounted on a stand tilted 16.2°. A WR5 probe is used to measure the near-fields on the plane S_{NF} which is d_p away from the top of the lens (see the inset). (b) Gain measurement: a standard WR5 horn antenna is placed d_h from the top of the lens. In both the measurements, absorbers were installed around the lens antenna, the probe, and the horn antenna to suppress multiple reflections, but they are not visible in the figure.

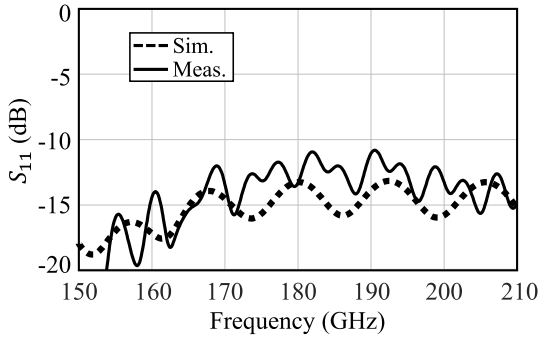

Fig. 18. Measured S_{11} of the fabricated lens antenna compared with the simulation where the same structure was modeled.

from a square waveguide to a standard WR5 waveguide flange, and the shaped quartz lens with the air cavity [see Fig. 16(c) and (d)]. The waveguide block and the double-slot iris are the same as those in [24] and operate from 140 to 220 GHz. The feed is displaced $\vec{d}_a = +1.8\hat{x}$ mm with respect to the lens apex as shown in Fig. 16(c), and it is aligned with the lens using two metal pins. The whole structure is assembled using four screws at the lens edges.

The quartz material was provided by Heraeus Group [35] (Suprasil 3001 Quartz material series) with homogeneous permittivity of $\varepsilon_r = 3.75$ and dielectric loss of $\tan\delta = 4.2 \times 10^{-4}$, over the considered frequency band. These values were measured for various quartz samples using our near-field measurement setup before fabrication. The shaped quartz lens was fabricated by LouwersHanique using their selective laser etching technique [36]. The lens surface was measured by the same company using an interferometer. The lens profiles along the main planes are shown in Fig. 16(c) and (d), compared with the designed ones in Fig. 11. The agreement is excellent and the surface difference meets the expectation

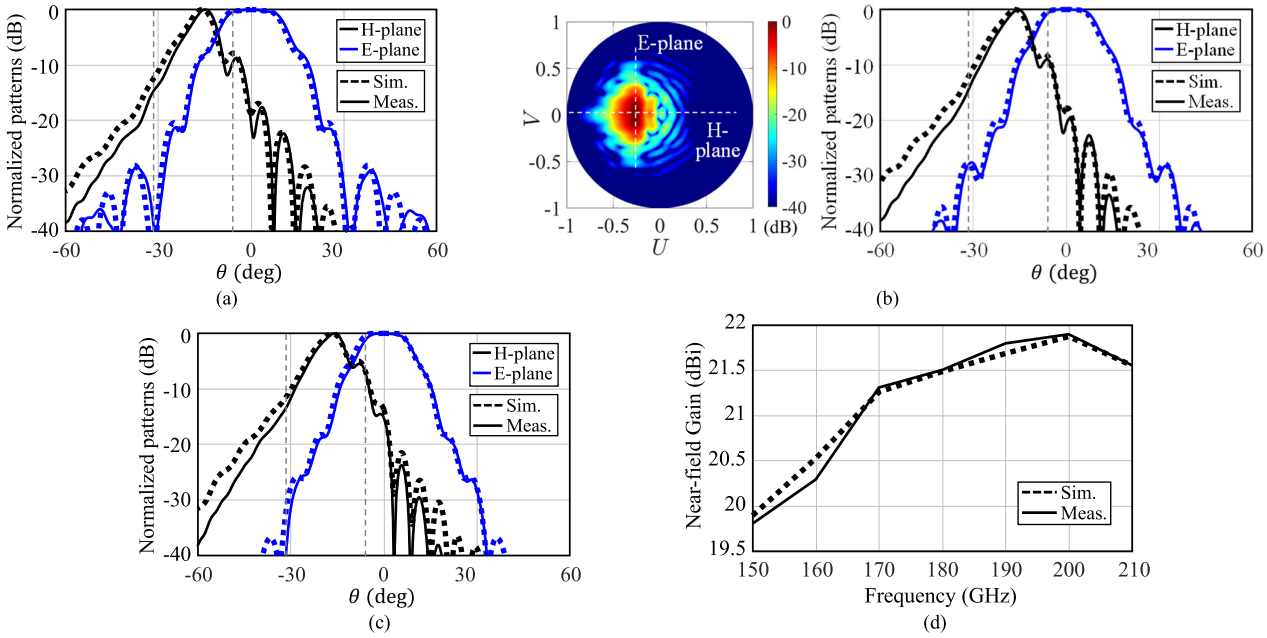

Fig. 19. Measured co-pol far-fields at (a) 160 GHz, (b) 180 GHz (the pattern in the UV plane is also shown), and (c) 200 GHz. The dashed gray lines mark the rim angles of the reflector in the H-plane. (d) Measured near-field gain when $d_h = 96.5$ mm. The impedance mismatch loss and the conductor loss in the waveguide are not included in the gain.

within ± 40 μm. Here to facilitate the fabrication of the first prototype, the matching layer is not included. As will be discussed in the following, this will decrease the system aperture efficiency by about 0.5 dB, but the SL remains the same. The measured reflection coefficient is below -10 dB over the considered frequency band with small oscillations. Therefore, it may not be necessary to implement a matching layer for certain applications.

B. Near-Field Measurement

The prototype was measured at TU Delft using the measurement setup shown in Fig. 17. The lens antenna is fed by a VNA extender from Virginia Diodes (WR5.1-VNAX) through a waveguide twist (to rotate the polarization). The extender is mounted on a 3-D-printed plastic stand which has a tilt angle of 16.2°. This angle corresponds to the main beam angle of the lens secondary field at 180 GHz (see Fig. 13). Using such a stand, the secondary field will point at 0° and its polarization will be parallel to the ground. This facilitates the near-field measurement over a plane parallel to the ground.

This setup was calibrated using a TRL kit, and the reference planes of both the waveguide ports are shown in Fig. 17(a). The measured reflection coefficient of the lens antenna is shown in Fig. 18 and compared with the simulation where the same structure was modeled. The measured S_{11} is below -10 dB over the considered frequency band agreeing very well with the simulation. If a matching layer is implemented, the oscillations in S_{11} will be further reduced; see Fig. 2(b).

The far-field patterns of the lens antenna are obtained from the planar near-field measurement where a WR5 probe is used. The probe scans a square plane S_{NF} at the top of the lens with the area of 40 mm $\times$ 40 mm and the distance of $d_p = 11.5$ mm, as depicted in the inset in Fig. 17(a). The position of the probe is controlled by a CNC scanner with a step size of 0.3 mm. During the measurement, the probe and the lens antenna were surrounded by absorbers to suppress the multiple reflections between the lens and the laboratory's surroundings. By implementing the transformation from near-fields to far-fields at each frequency, the corresponding co-pol far-field patterns at 160, 180, and 200 GHz are shown in Fig. 19(a)–(c) along the main planes and compared with the simulations. The agreement is excellent in both the planes at all the frequencies, and the difference in the main beam position is less than 0.8°.

The realized gain is quantified resorting to the Friis equation and the measured coupling coefficient S_{12} between the lens antenna and a standard WR5 horn antenna shown in Fig. 17(b). The horn is placed $d_h = 96.5$ mm away from the lens top and was surrounded by absorbers during the measurement. The realized gain considers the measured S_{11} in Fig. 18, the dielectric loss in quartz, and the conductor loss in the waveguide, which are listed in Table II. The dielectric loss is estimated to be 0.2–0.3 dB from 150 to 210 GHz. The waveguide was fabricated at the workshop at TU Delft with very high metal roughness, leading to an equivalent low metal conductivity of 3.6×10^5 S/m, as discussed in [24]. The total length of the waveguide is about 1.4 cm and the simulated waveguide loss is from 1.4 to 1 dB (150–210 GHz). This loss can be significantly decreased using a low-roughness metallization with a much higher equivalent conductivity, e.g., 3.6×10^7 S/m, as shown in Table II. By removing the measured impedance mismatch loss and the conductor loss from the realized gain, we can obtain the near-field gain of the lens antenna evaluated at $d_h = 96.5$ mm. It is shown in Fig. 19(d) as a function of frequencies and is compared with the simulation. The measured gain is comparable to the simulated one with maximum difference of 0.2 dB over the

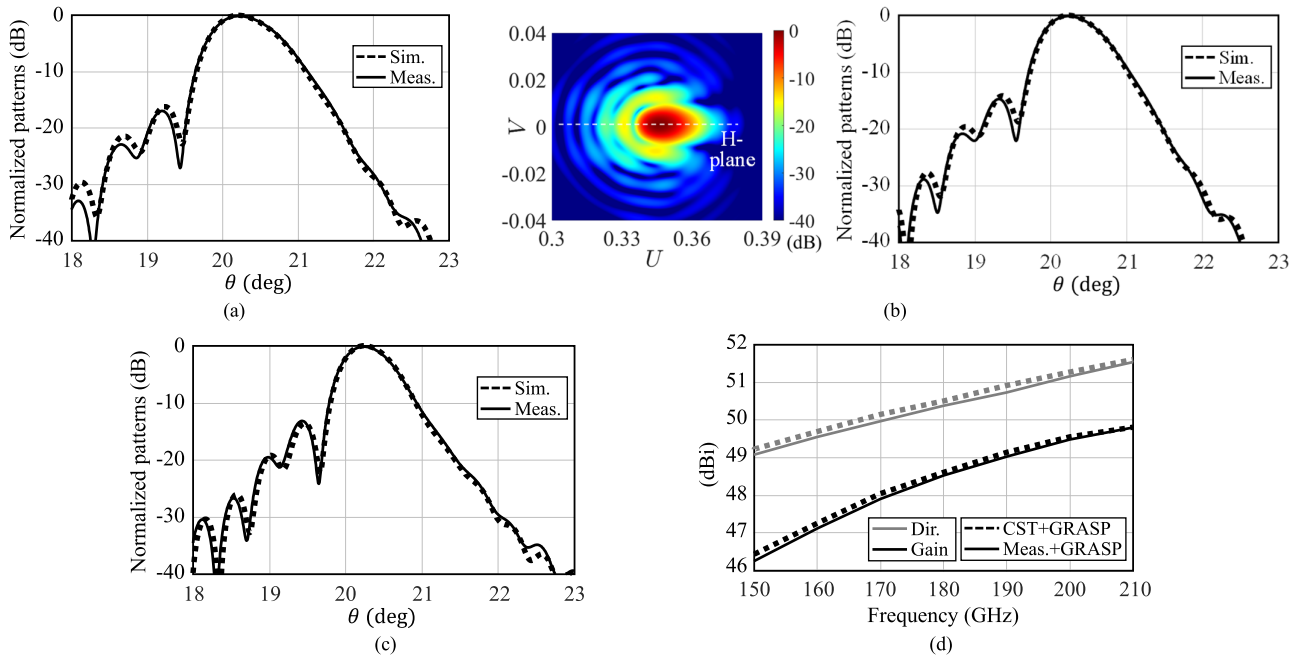

Fig. 20. GRASP simulations of the reflector's co-pol far-fields in the H-plane at (a) 160 GHz, (b) 180 GHz (the pattern in the UV plane is also shown), and (c) 200 GHz. In GRASP, the measured and simulated lens far-fields are imported as a tabulated source. (d) Directivity and gain of the lens-coupled reflector.

TABLE II
LOSS TERMS RELEVANT TO THE PROTOTYPE FROM 150 TO 210 GHZ

Frequency (GHz)	Waveguide (dB) 3.6×10^7 S/m	Waveguide (dB) 3.6×10^5 S/m	Dielectric (dB)	Mismatch (dB)
150	0.14	1.38	0.19	0.16
180	0.11	1.06	0.23	0.2
210	0.1	0.99	0.27	0.14

entire frequency band. This difference is associated with the fabrication and measurement tolerances, and the estimation of the conductor loss.

Moreover, we import the measured far-fields into GRASP as a tabulate source to evaluate the far-fields radiated by the reflector. The source position is the same as that in the measurement setup. Fig. 20(a)–(c) shows the reflector's co-pol far-fields in the H-plane at 160, 180 (the pattern in the UV plane is also shown), and 200 GHz, respectively. The measured far-fields almost overlap with the simulations, showing excellent agreement. The directivity and the gain of the reflector are plotted in Fig. 20(d). The measurement is less than 0.2 dB different from the simulation. Note that the simulated gain at 180 GHz is slightly lower than that in Fig. 14 since the matching layer is not implemented (the directivity remains the same). In this case, the simulated aperture efficiency drops about 0.5 dB to $\eta_{ap}^{CST+GRASP} = 37.1\%$, which corresponds to the drop in the lens radiation efficiency. For lenses without the matching layers, their simulated SL remains the same as that in Fig. 7.

VII. CONCLUSION

FPAs based on dielectric lenses with LWA feeds are promising candidates for large-format and wide field-of-view imaging systems at submillimeter wavelengths. In this work, we consider quartz lenses coupled to a parabolic reflector and focus on optimizing the scanning gain of such a system when the scanning angles are large, via shaping the quartz lens surfaces. We have proposed an optimization procedure using a field correlation technique at the top of the lens. Once the incident reflector's focal fields and the lens radiated fields on the same plane are conjugately matched, we can obtain the lowest SL for the system.

When the scanning angles are large, lens elements can be located outside the rim of the reflector, and the reflector's focal fields can present significant higher order phase terms. To match with these phase terms, we have discussed the method to modify the shape of the lens surface and thus modify the phase propagation of the lens radiated fields. In fact, the field correlation approach directly provides the hologram phase to be synthesized by the surface modification. The shaped lens is then expanded into the Zernike polynomials leading to a smoother practical surface. We have shown an example of shaped lens design operating at 180 GHz for an extreme case when the reflector scans 20.3° (50 beams). The far-field performance obtained from our approach is in excellent agreement with the full-wave simulations. The latter achieves 50.5-dBi directivity with 2.6-dB scanning gain loss which is much lower than that of the reflector's focal field (about 6 dB).

To validate the simulations, we have fabricated and measured this shaped quartz lens. The fabricated lens surface presents very good surface difference (± 40 μm) compared with the designed one. The measured reflection coefficient

is less than −10 dB from 150 to 210 GHz. The measured lens near-fields, when propagated to the far-field region, point toward the expected angular position and are in excellent agreement with the full-wave simulations over the entire frequency band. We have also evaluated the reflector's far-fields when using the lens far-fields calculated from the measured near-field data as the source in GRASP. The resulting far-fields also present excellent agreement with the simulations, validating the proposed method for shaping dielectric lens surfaces.

REFERENCES

[1] M. J. Griffin et al., "The Herschel-SPIRE instrument and its in-flight performance," *Astron. Astrophys.*, vol. 518, p. L3, Jul. 2010.

[2] K. B. Cooper, R. J. Dengler, N. Llombart, B. Thomas, G. Chattopadhyay, and P. H. Siegel, "THz imaging radar for standoff personnel screening," *IEEE Trans. THz Sci. Technol.*, vol. 1, no. 1, pp. 169–182, Sep. 2011.

[3] J. Leech, B. K. Tan, G. Yassin, P. Kittara, and S. Wangsuya, "Experimental investigation of a low-cost, high performance focal-plane horn array," *IEEE Trans. THz Sci. Technol.*, vol. 2, no. 1, pp. 61–70, Jan. 2012.

[4] R. Al Hadi et al., "A 1 k-Pixel video camera for 0.7–1.1 terahertz imaging applications in 65-nm CMOS," *IEEE J. Solid-State Circuits*, vol. 47, no. 12, pp. 2999–3012, Dec. 2012.

[5] G. C. Trichopoulos, H. L. Mosbacker, D. Burdette, and K. Sertel, "A broadband focal plane array camera for real-time THz imaging applications," *IEEE Trans. Antennas Propag.*, vol. 61, no. 4, pp. 1733–1740, Apr. 2013.

[6] E. Heinz et al., "Progress in passive submillimeter-wave video imaging," *Proc. SPIE*, vol. 9078, Jun. 2014, Art. no. 907808.

[7] S. van Berkel, O. Yurduseven, A. Freni, A. Neto, and N. Llombart, "THz imaging using uncooled wideband direct detection focal plane arrays," *IEEE Trans. THz Sci. Technol.*, vol. 7, no. 5, pp. 481–492, Sep. 2017.

[8] D. A. Robertson et al., "The CONSORTIS 16-channel 340-GHz security imaging radar," *Proc. SPIE*, vol. 10634, May 2018, Art. no. 1063409.

[9] A. Dubok, A. Al-Rawi, G. Gerini, and A. B. Smolders, "Reflector synthesis for wide-scanning focal plane arrays," *IEEE Trans. Antennas Propag.*, vol. 67, no. 4, pp. 2305–2319, Apr. 2019.

[10] J. J. A. Baselmans et al., "A kilo-pixel imaging system for future space based far-infrared observatories using microwave kinetic inductance detectors," *Astron. Astrophys.*, vol. 601, p. A89, May 2017.

[11] E. Gandini, J. Svedin, T. Bryllert, and N. Llombart, "Optomechanical system design for dual-mode stand-off submillimeter wavelength imagers," *IEEE Trans. THz Sci. Technol.*, vol. 7, no. 4, pp. 393–403, Jul. 2017.

[12] E. Gandini and N. Llombart, "Toward a real time stand-off submillimeter-wave imaging system with large field of view: Quasi-optical system design considerations," *Proc. SPIE*, vol. 9462, May 2015, Art. no. 946205.

[13] B. Chantraine-Bares, R. Sauleau, L. Le Coq, and K. Mahdjoubi, "A new accurate design method for millimeter-wave homogeneous dielectric substrate lens antennas of arbitrary shape," *IEEE Trans. Antennas Propag.*, vol. 53, no. 3, pp. 1069–1082, Mar. 2005.

[14] R. Sauleau and B. Bares, "A complete procedure for the design and optimization of arbitrarily shaped integrated lens antennas," *IEEE Trans. Antennas Propag.*, vol. 54, no. 4, pp. 1122–1133, Apr. 2006.

[15] G. Godi, R. Sauleau, L. L. Coq, and D. Thouroude, "Design and optimization of three-dimensional integrated lens antennas with genetic algorithm," *IEEE Trans. Antennas Propag.*, vol. 55, no. 3, pp. 770–775, Mar. 2007.

[16] B. Chantraine-Bares and R. Sauleau, "Electrically-small shaped integrated lens antennas: A study of feasibility in *Q*-band," *IEEE Trans. Antennas Propag.*, vol. 55, no. 4, pp. 1038–1044, Apr. 2007.

[17] A. Rolland, M. Ettorre, A. V. Boriskin, L. Le Coq, and R. Sauleau, "Axisymmetric resonant lens antenna with improved directivity in Ka-band," *IEEE Antennas Wireless Propag. Lett.*, vol. 10, pp. 37–40, 2011.

[18] T. Dang, J. Yang, and H.-X. Zheng, "An integrated lens antenna design with irregular lens profile," in *Proc. 5th Global Symp. Millim.-Waves*, Harbin, China, May 2012, pp. 212–215.

[19] T. Jaschke, B. Rohrdantz, and A. F. Jacob, "A flexible surface description for arbitrarily shaped dielectric lens antennas," in *Proc. GeMiC German Microw. Conf.*, Aachen, Germany, Mar. 2014, pp. 1–4.

[20] L. Mescia, P. Bia, D. Caratelli, M. A. Chiapperino, O. Stukach, and J. Gielis, "Electromagnetic mathematical modeling of 3D supershaped dielectric lens antennas," *Math. Problems Eng.*, vol. 2016, pp. 1–10, Feb. 2016.

[21] C. C. Cruz, J. R. Costa, C. A. Fernandes, and S. A. Matos, "Focal-plane multibeam dual-band dielectric lens for Ka-band," *IEEE Antennas Wireless Propag. Lett.*, vol. 16, pp. 432–436, 2017.

[22] S. O. Dabironezare, G. Carluccio, A. Freni, A. Neto, and N. Llombart, "Coherent Fourier optics model for the synthesis of large format lens-based focal plane arrays," *IEEE Trans. Antennas Propag.*, vol. 69, no. 2, pp. 734–746, Feb. 2021.

[23] N. Llombart, G. Chattopadhyay, A. Skalare, and I. Mehdi, "Novel terahertz antenna based on a silicon lens fed by a leaky wave enhanced waveguide," *IEEE Trans. Antennas Propag.*, vol. 59, no. 6, pp. 2160–2168, Jun. 2011.

[24] M. Arias Campo, D. Blanco, S. Bruni, A. Neto, and N. Llombart, "On the use of Fly's eye lenses with leaky-wave feeds for wide-band communications," *IEEE Trans. Antennas Propag.*, vol. 68, no. 4, pp. 2480–2493, Apr. 2020.

[25] *CST Microwave Studio*. Accessed: 2022. [Online]. Available: http://www.cst.com

[26] L. W. Mou, Y. J. Cheng, Y. F. Wu, M. H. Zhao, and H. N. Yang, "Design for array-fed beam-scanning reflector antennas with maximum radiated power efficiency based on near-field pattern synthesis by support vector machine," *IEEE Trans. Antennas Propag.*, vol. 70, no. 7, pp. 5035–5043, Jul. 2022.

[27] V. Rumsey, "On the design and performance of feeds for correcting spherical aberration," *IEEE Trans. Antennas Propag.*, vol. AP-18, no. 3, pp. 343–351, May 1970.

[28] H. Zhang, S. O. Dabironezare, G. Carluccio, A. Neto, and N. Llombart, "A Fourier optics tool to derive the plane wave spectrum of quasi-optical systems [EM programmer's notebook]," *IEEE Antennas Propag. Mag.*, vol. 63, no. 1, pp. 103–116, Feb. 2021.

[29] S. Bosma, A. Neto, and N. Llombart, "On the near-field spherical wave formation in resonant leaky-wave antennas: Application to small lens design," *IEEE Trans. Antennas Propag.*, vol. 70, no. 2, pp. 801–812, Feb. 2022.

[30] *TICRA Tools GRASP*. Accessed: 2022. [Online]. Available: https://www.ticra.com/software/grasp

[31] F. Zernike, "Beugungstheorie des Schneidenverfahrens und Seiner Verbesserten Form, der Phasenkontrastmethode," *Physica*, vol. 1, nos. 7–12, pp. 689–704, 1934.

[32] A. N. Plastikov, "A high-gain multibeam bifocal reflector antenna with 40° field of view for satellite ground station applications," *IEEE Trans. Antennas Propag.*, vol. 64, no. 7, pp. 3251–3254, Jul. 2016.

[33] E. Gandini, A. Tamminen, A. Luukanen, and N. Llombart, "Wide field of view inversely magnified dual-lens for near-field submillimeter wavelength imagers," *IEEE Trans. Antennas Propag.*, vol. 66, no. 2, pp. 541–549, Feb. 2018.

[34] E. Martinez-de-Rioja, J. A. Encinar, A. G. Pino, B. Gonzalez-Valdes, S. V. Hum, and C. T. Herrero, "Bifocal design procedure for dual-reflectarray antennas in offset configurations," *IEEE Antennas Wireless Propag. Lett.*, vol. 17, no. 8, pp. 1421–1425, Aug. 2018.

[35] Hanau, Germany. *Heraeus Group*. Accessed: 2022. [Online]. Available: https://www.heraeus.com/media/media/hca/doc_hca/products_and_solutions_8/optics/Data_and_Properties_Optics_fused_silica_EN.pdf

[36] The Netherlands. *Laser Processing of Optical Components LouwersHanique*. Accessed: 2022. [Online]. Available: https://www.louwershanique.com/services/laser-processing

Huasheng Zhang (Member, IEEE) received the B.Eng. degree (cum laude) in electronic information engineering from Beihang University, Beijing, China, in 2016, and the M.Sc. degree (cum laude) in electrical engineering from the Delft University of Technology (TU Delft), Delft, The Netherlands, in 2018, where he is currently pursuing the Ph.D. degree with the Terahertz Sensing Group.

His research interests include analyzing and designing leaky-wave antennas, lens antennas, photoconductive antennas, and quasi-optical systems at millimeter and submillimeter wavelengths, and high-frequency electromagnetic analysis techniques.

Shahab Oddin Dabironezare (Member, IEEE) was born in Mashhad, Iran. He received the M.Sc. and Ph.D. degrees in electrical engineering from the Delft University of Technology, Delft, The Netherlands, in 2015 and 2020, respectively.

From 2020 to 2022, he was a Post-Doctoral Researcher with the Microelectronics Department, Terahertz (THz) Sensing Group, TU Delft. He is currently an Assistant Professor at the THz Sensing Group, TU Delft, and an Instrument Scientist at the Netherlands Institute for Space Research (SRON), Leiden, The Netherlands. His research interests include wideband antennas at millimeter- and submillimeter-wave applications, wide field-of-view imaging systems, quasi-optical systems, lens antennas, and absorber-based detector systems.

Jochem J. A. Baselmans was born in 1974. He received the Graduate and Ph.D. degrees (summa cum laude) from the University of Groningen, Groningen, The Netherlands, in 1998 and 2002, respectively. His doctoral dissertation was entitled "Controllable Josephson Junctions."

He started in 2002 as a Post-Doctoral Instrument Scientist at the SRON Netherlands Institute for Space Research, Leiden, The Netherlands, where he has worked until 2004 in hot electron bolometer mixers. In 2005, he moved to SRON Utrecht and started working on Microwave Kinetic Inductance Detectors (MKIDs), after a three-month visit to the California Institute of Technology, Pasadena, CA, USA. From 2012 to 2015, he was the Work-Package Leader of the FP7 Project Spacekids. He is currently a Senior Instrument Scientist at the SRON Netherlands Institute for Space Research, where he has worked since 2002 with the Technology Division. He is also a Full Professor in experimental astronomy at the THz Sensing Group, Delft University of Technology, Delft, The Netherlands, since 2019. He had published more than 130 articles. He now leads the Dutch effort on the development of MKIDs, where his main interests are ultrasensitive MKIDs for THz radiation, detection, and advanced on-chip imaging spectrometers for sub-THz imaging spectroscopy.

Dr. Baselmans received an ERC Consolidator Grant to develop an advanced imaging spectrometer based on MKIDs in 2015.

Nuria Llombart (Fellow, IEEE) received the master's degree in electrical engineering and the Ph.D. degree from the Polytechnic University of Valencia, Valencia, Spain, in 2002 and 2006, respectively.

During her master's degree studies, she spent one year at the Friedrich-Alexander University of Erlangen-Nuremberg, Erlangen, Germany, and worked at the Fraunhofer Institute for Integrated Circuits, Erlangen. From 2002 to 2007, she was with the Antenna Group, TNO Defense, Security and Safety Institute, The Hague, The Netherlands, working as a Ph.D. Student and afterward as a Researcher. From 2007 to 2010, she was a Post-Doctoral Fellow with the California Institute of Technology, Pasadena, CA, USA, working with the Submillimeter Wave Advance Technology Group, Jet Propulsion Laboratory, Pasadena. She was a "Ramón y Cajal" Fellow with the Department of Optics, Complutense University of Madrid, Madrid, Spain, from 2010 to 2012. In September 2012, she joined the THz Sensing Group, Delft University of Technology, Delft, The Netherlands, where she has been a Full Professor, since February 2018. She has coauthored more than 150 journals and international conference contributions. Her research interests include analysis and design of planar antennas, periodic structures, reflector antennas, lens antennas, and waveguide structures, with an emphasis on the THz range.

Dr. Llombart serves as a Board Member for the IRMMW-THz International Society. She was a recipient of the H. A. Wheeler Award for the Best Applications Paper of 2008 from the IEEE TRANSACTIONS ON ANTENNAS AND PROPAGATION, the 2014 THz Science and Technology Best Paper Award from the IEEE Microwave Theory and Techniques Society, the 2014 IEEE Antenna and Propagation Society Lot Shafai Mid-Career Distinguished Achievement Award, the European Research Council Starting Grant in 2015, and several NASA awards.